Far-field sensitivity to local boundary perturbations in 2D wave scattering

E. García Neefjes[1] S. C. Hawkins[2]

(Received 20 February 2025; revised 9 September 2025)

Abstract

We numerically investigate the sensitivity of the scattered wave field to perturbations in the shape of a 2D sound-soft scattering body illuminated by an incident plane wave. This study is motivated by recent work on the inverse problem of reconstructing a scatterer shape from measurements of the scattered wave at large distances from the scatterer. For this purpose we consider star-shaped scatterers represented using cubic splines, and our approach is based on a Nyström method-based discretisation of the shape derivative. Using singular value decomposition, we identify fundamental geometric modes that most strongly influence the scattered wave, providing insight into the most visible boundary features in scattering data.

DOI:10.21914/anziamproc.v66.19625, © Austral. Mathematical Soc. 2025. Published 2025-12-08, as part of the Proceedings of the 22nd Biennial Computational Techniques and Applications Conference. ISSN 1445-8810. (Print two pages per sheet of paper.) Copies of this article must not be made otherwise available on the internet; instead link directly to the DOI for this article.

Contents

1 Introduction

When a wave interacts with a *scatterer*, its properties are modified through a process known as *wave scattering* [2]. The scattered wave pattern depends strongly on the shape and properties of the scatterer and the direction from which the wave approaches. Of particular interest is the response of the scattered wave at large distances from the scatterer, commonly known as the *far-field*. In this region, the 2D scattered wave approximates an outgoing cylindrical wave, with its amplitude decreasing inversely with the square root of distance from the scatterer. Far-field patterns are important in practice since often measurements must be made at considerable distances from the scattering object. Given far-field measurements, reconstructing properties of the scatterer is a classical *ill-posed* inverse problem. While the forward map from scatterers to far-fields has no inverse, various methods, including iterative Newton-type algorithms, qualitative methods such as the linear sampling method, and Tikhonov regularization approaches, have been developed to obtain approximate reconstructions of the scatterer geometry [3].

For the inverse shape problem, remarkable reconstructions have been obtained with (deterministic) regularized Newton-type methods [1], as well as (stochastic) Bayesian counterparts [8]. In tackling this problem, following Ganesh et al. [5], we observed that certain geometric features of the scatterer boundary are much more readily reconstructible from far-field data than others, with some features appearing essentially invisible to far-field measurements. In this article, we investigate these phenomena further by considering the forward problem for an illustrative geometry, and show how our previous observations can be explained via analysis of the shape-derivative. Interpreting this derivative is facilitated by Singular Value Decomposition (SVD), which allows identification of the geometric perturbation modes that are most *visible* in the far-field, and hence expected to be *reconstructible* in the inverse problem configuration.

Unlike traditional approaches which use global basis functions like *Karhunen-Loève* expansions [8, 5], the use of cubic splines allows for localised geometric perturbations, which is particularly valuable for understanding how specific geometric features influence the far-field. However, for such analysis it is paramount to be able to generate accurate numerical solutions, especially for complicated shapes with high spatial resolution. We overcome this by using the spectral *Nyström* method [3] for solving Boundary Integral Equations (BIEs), and we ensure the required smoothness of our scatterer's boundary representation.

In Section 2 we present the class of scatterers considered in this article. Section 3 focuses on the wave scattering model including the governing BIEs that lead to the sensitivity matrix. In Section 4 we demonstrate our corresponding numerical results with a focus on the SVD analysis. Conclusions are given in Section 5.

2 Scatterer representation: splines

Let $\mathsf{D}(\boldsymbol{\omega}) \subset \mathbb{R}^2$ denote the simply connected region occupied by the scatterer, where $\boldsymbol{\omega}$ denotes a vector characterising the domain D. We assume that $\mathsf{D}(\boldsymbol{\omega})$ is *star-shaped* with centre at the origin (see Figure 1), and use polar coordinates to parametrise its boundary $\partial\mathsf{D}(\boldsymbol{\omega})$ through the continuous map

$\chi : [0, 2\pi) \to \partial D(\omega)$ given by

$$\chi(\theta) = r(\theta)\hat{e}_r(\theta)\,, \quad \theta \in [0, 2\pi)\,, \tag{1}$$

where $r(\theta) > 0$, and $\hat{e}_r(\theta) = \cos\theta\hat{e}_x + \sin\theta\hat{e}_y$ represents the (unit) vector in the radial direction, and $\hat{e}_x$ and $\hat{e}_y$ are the constant Cartesian unit vectors. The closedness of the boundary implies that $\chi(0) = \chi(2\pi)$.

We are interested in a class of scatterers in which the *log-radius* $s(\theta)$, satisfying

$$r(\theta) = e^{s(\theta)}\,, \tag{2}$$

is a cubic spline utilising piecewise C^2 polynomials and periodic end conditions, so that

$$s(\theta) = \sum_{j=1}^{N_{\text{spline}}} a_j(\omega)(\theta - \theta_j^{\partial D})^3 + b_j(\omega)(\theta - \theta_j^{\partial D})^2 + c_j(\omega)(\theta - \theta_j^{\partial D}) + d_j(\omega)\,, \tag{3}$$

for $\theta \in [\theta_j^{\partial D}, \theta_{j+1}^{\partial D})$. The equispaced knots are $\theta_j^{\partial D} = 2\pi(j-1)/N_{\text{spline}}$ for $j = 1, \ldots, N_{\text{spline}}$. In practice, the values $d_i \equiv s(\theta_i^{\partial D})$ for $i = 1, \ldots, N_{\text{spline}}$ of the log-radius at the knots are sufficient to uniquely describe the scatterer, and without loss of generality we can write the vector of coefficients $\mathbf{d}(\omega) = \omega \in \mathbb{R}^{N_{\text{spline}}}$. Coefficients $\mathbf{a}(\omega)$, $\mathbf{b}(\omega)$ and $\mathbf{c}(\omega)$ in (3) are obtained by solving an associated linear system where only the right hand side depends on ω. Figure 1 depicts the 'Australia' reference shape and the corresponding scatterers obtained using the construction (3) with $N_{\text{spline}} = 12, 48$ interpolation points.

3 Scattering model for sensitivity analysis

We consider time-harmonic waves with angular frequency ψ propagating in a non-dispersive homogeneous medium with constant wave speed c exterior to $D(\omega)$. The respective waves are described by the complex valued function $u(x;\omega)$, which satisfies the 2D Helmholtz equation

$$\left(\Delta + k^2\right) u(x;\omega) = 0\,, \quad x \in \mathbb{R}^2 \setminus \overline{D}(\omega)\,, \tag{4}$$

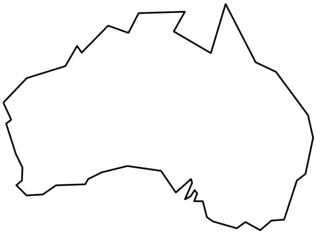

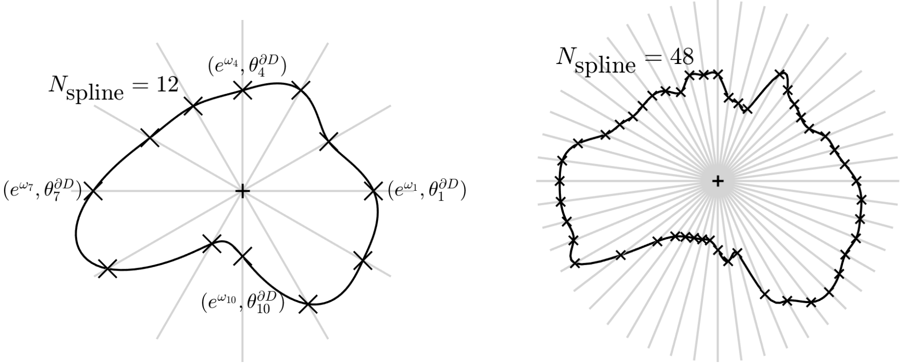

Figure 1: (left) Visualisation of our reference scatterer, a polygonal approximation to the coast of mainland Australia. (bottom) Star-shaped cubic spline scatterer approximations $D(\boldsymbol{\omega})$ to the reference shape for $N_{\text{spline}} = 12, 48$. The "+" symbol represents the scatterers centre and the "×" visualise the knots and their associated data. The left scatter plot includes reference $(r, \theta^{\partial D})$ boundary values.

where $k = \psi/c$ denotes the wavenumber. The waves are forced by an *incident* plane wave

$$u^{\text{inc}}(\mathbf{x}) = e^{ik\mathbf{x}\cdot\widehat{\mathbf{d}}}, \tag{5}$$

travelling in the direction of the (unit) vector $\widehat{\mathbf{d}}$, which induces a *scattered* field u^{sc}. The scattered field must additionally satisfy the radiation condition [7]

$$\frac{\partial u^{\text{sc}}}{\partial r}(\mathbf{x};\boldsymbol{\omega}) - iku^{\text{sc}}(\mathbf{x};\boldsymbol{\omega}) = o\left(|\mathbf{x}|^{-1/2}\right), \quad \text{as} \quad |\mathbf{x}| \to \infty, \tag{6}$$

uniformly with respect to direction $\hat{\mathbf{x}} = \mathbf{x}/|\mathbf{x}| = \hat{\mathbf{e}}_r(\theta) \in \partial B$, where $\partial B \subseteq \mathbb{R}^2$ denotes the set of all directions in the unit circle. Here (r, θ) denotes the polar coordinate representation of $\mathbf{x}$. The radiation condition (6) allows us to introduce the far-field pattern $u^\infty(\hat{x};\omega)$ induced as a result of the interaction of an incident plane wave with the particle $D(\omega)$ via [e.g. 3, eq. 3.109]

$$u^{sc}(x;\omega) = \frac{e^{ik|x|}}{\sqrt{|x|}}\left[u^\infty(\hat{x};\omega) + O\left(\frac{1}{|x|}\right)\right], \quad \text{as} \quad |x| \to \infty\,. \tag{7}$$

For a fixed incident plane wave, it is convenient to introduce the far-field operator $\mathcal{F} : C([0, 2\pi)) \to C(\partial B)$ by

$$\mathcal{F}r(\theta,\omega) = u^\infty(\hat{x};\omega)\,, \tag{8}$$

which maps the boundary ∂D (defined using r) of the sound-soft scatterer onto the far-field pattern of the scattered wave. For a sound-soft scatterer with Dirichlet boundary conditions on the boundary $\partial D(\omega)$, we have

$$u(x;\omega) = f \quad \text{for } x \in \partial D(\omega)\,, \tag{9}$$

with $f = 0$. Although our analysis below is focused on sound-soft scatterers following Colton and Kress [3, Section 5.3], similar results can be obtained for the Neumann problem and more general boundary conditions [6].

An efficient way to evaluate $\mathcal{F}$ when $f = 0$ is to use the BIE reformulation

$$(\mathcal{I} + 2\mathcal{K}' - ik\mathcal{S})\,\frac{\partial u}{\partial n} = 2\frac{\partial u^{inc}}{\partial n} - iku^{inc}\,, \quad x \in \partial D(\omega)\,, \tag{10}$$

where $\mathcal{I}$ is the identity operator, $\mathcal{S}$ is the single-layer potential, and $\mathcal{K}'$ is the double-layer transpose potential [3]. The unknown in (10) is the physical-quantity $\partial u/\partial n = \nabla u \cdot n$, where $n(x_0)$ denotes the outward unit normal to $\partial D(\omega)$ at x_0. Once $\partial u/\partial n$ has been computed by solving (10), we compute the scattered field away from the boundary as

$$u^{sc} = -\mathcal{S}\frac{\partial u}{\partial n} \quad \text{for } x \in \mathbb{R}^2 \setminus \overline{D}(\omega)\,.$$

The far-field can then be computed similarly.

We compute high-order approximate solutions to the wave-scattering problem introduced above using a spectral Nyström method, implemented in open source software [4], in which equation (10) is discretized using $2m+2$ equispaced points on the boundary $\partial D(\boldsymbol{\omega})$, with m the Nyström parameter of Colton and Kress [3], leading to a linear system

$$\mathbf{A}(\boldsymbol{\omega})\boldsymbol{\phi}(\boldsymbol{\omega}) = \mathbf{b}\,, \tag{11}$$

where the matrix $\mathbf{A}(\boldsymbol{\omega})$ represents the discretization of the combined field integral operators on the left hand side of (10), $\mathbf{b}$ contains samples of the right hand side of (10) evaluated at the discretization points, and $\boldsymbol{\phi}$ approximates $\partial u/\partial n$ at these points. We emphasise that, because the integration in (10) is over the boundary ∂D, the matrix $\mathbf{A}(\boldsymbol{\omega})$ must be recomputed for each new scatterer configuration.

Next we examine the sensitivity of the far-field to changes in the scatterer's shape, by considering the partial derivatives of the mapping $\mathcal{F} : r(\theta;\boldsymbol{\omega}) \mapsto u^\infty$. Using the chain rule gives

$$J_i = \frac{\partial \mathcal{F}}{\partial \omega_i} = \frac{d\mathcal{F}}{dr}\left(\frac{\partial r}{\partial \omega_i}\right), \quad \frac{\partial r}{\partial \omega_i} = r(\theta)\frac{\partial s(\theta;\boldsymbol{\omega})}{\partial \omega_i}\,. \tag{12}$$

Here $d\mathcal{F}(\cdot)/dr$ is the *Fréchet derivative* of $\mathcal{F}$. The Fréchet derivative is given by the far-field of an auxiliary wave field v satisfying (4), (6) and the inhomogeneous Dirichlet condition [see 3, Theorem 5.15]

$$v(\mathbf{x};\boldsymbol{\omega}) = -\mathbf{n}\cdot[q(\theta)\hat{\mathbf{e}}_r(\theta)\circ\chi^{-1}]\frac{\partial u}{\partial n} \quad \text{for } \mathbf{x}\in\partial D(\boldsymbol{\omega})\,, \tag{13}$$

with $q \in \partial B$ a scalar function representing the direction. To compute v we solve the combined-field BIE [3, (3.29)] for ϕ^* where the inhomogeneity is coupled with (10),

$$(\mathcal{I} + 2\mathcal{K} + 2ik\mathcal{S})\phi^* = -2\mathbf{n}\frac{\partial u}{\partial n}\cdot[q(\theta)\hat{\mathbf{e}}_r(\theta)\circ\chi^{-1}]\,, \quad \mathbf{x}\in\partial D(\boldsymbol{\omega})\,. \tag{14}$$

Once the surface potential ϕ^* has been obtained by solving (14), we compute the induced field using $v(\mathbf{x}) = (\mathcal{K} + ik\mathcal{S})\phi^*$ for $\mathbf{x}\in\mathbb{R}^2\setminus\overline{D}(\boldsymbol{\omega})$. The far-field is computed similarly.

Remark 1. We use the BIE (10) to solve the forward scattering problem because it yields the surface potential $\partial u/\partial n$, which is required in the right hand side of (14) to compute the Fréchet derivative. The BIE (10) is not appropriate for solving the Fréchet derivative PDE subject to the Dirichlet data in (13), because the right hand side of (10) would require a further normal derivative of u; in this case the simpler indirect BIE (14) is preferred.

To better understand the sensitivity of the derivative to perturbations in the shape, we compute the singular value decomposition

$$\mathbf{J} = \mathbf{U}\boldsymbol{\Sigma}\mathbf{V}^\top\,, \tag{15}$$

where $J_{ij} = |J_i(\theta_j)|$ are the entries in the $N_{\text{spline}} \times N_{\text{obs}}$ sensitivity matrix, $\boldsymbol{\Sigma}$ is the $N_{\text{spline}} \times N_{\text{obs}}$ matrix of singular values $\sigma_i \geq 0$, $\mathbf{U} = [\mathbf{u}_1 \mid \mathbf{u}_2 \mid \cdots \mid \mathbf{u}_{N_{\text{spline}}}]$ is $N_{\text{spline}} \times N_{\text{spline}}$ with $\mathbf{u}_i$ the unit left singular vectors of $\mathbf{J}$, and $\mathbf{V} = [\boldsymbol{v}_1 \mid \boldsymbol{v}_2 \mid \cdots \mid \boldsymbol{v}_{N_{\text{obs}}}]$ is $N_{\text{obs}} \times N_{\text{obs}}$ with $\boldsymbol{v}_i$ the (unit) right singular vectors of $\mathbf{J}$. For multiple incident waves, we define $\mathcal{F}$ to be the concatenation of the mappings for each incident wave. Then an analogue of (15) applies and $\mathbf{J} \in \mathbb{R}^{N_{\text{spline}} \times (N_{\text{inc}} N_{\text{obs}})}$ is the reshaped sensitivity matrix including all incident directions. This is useful since, as we see below, it deemphasises the role of the incident wave direction in identifying the most significant geometric features contributing to the far-field.

4 Numerical results

We present results for the scatterers in the bottom row of Figure 1 with $N_{\text{spline}} = 12, 48$ to directly compare how geometric resolution affects sensitivity. From (3), it can be seen that the input function $q = \partial r/\partial\omega_i$ to the Fréchet operator (12) is itself a cubic spline whose values at the knots are $\partial s(\theta_i^{\partial D}; \boldsymbol{\omega})/\partial\omega_i = \boldsymbol{e}_i$. It follows that the associated perturbation of the shape is localised around ω_i, as is illustrated in Figure 2 (top-left).

We let a be the diameter of the smallest ball circumscribing the scatterer and present our results in terms of the non-dimensional frequency ka. Figure 2

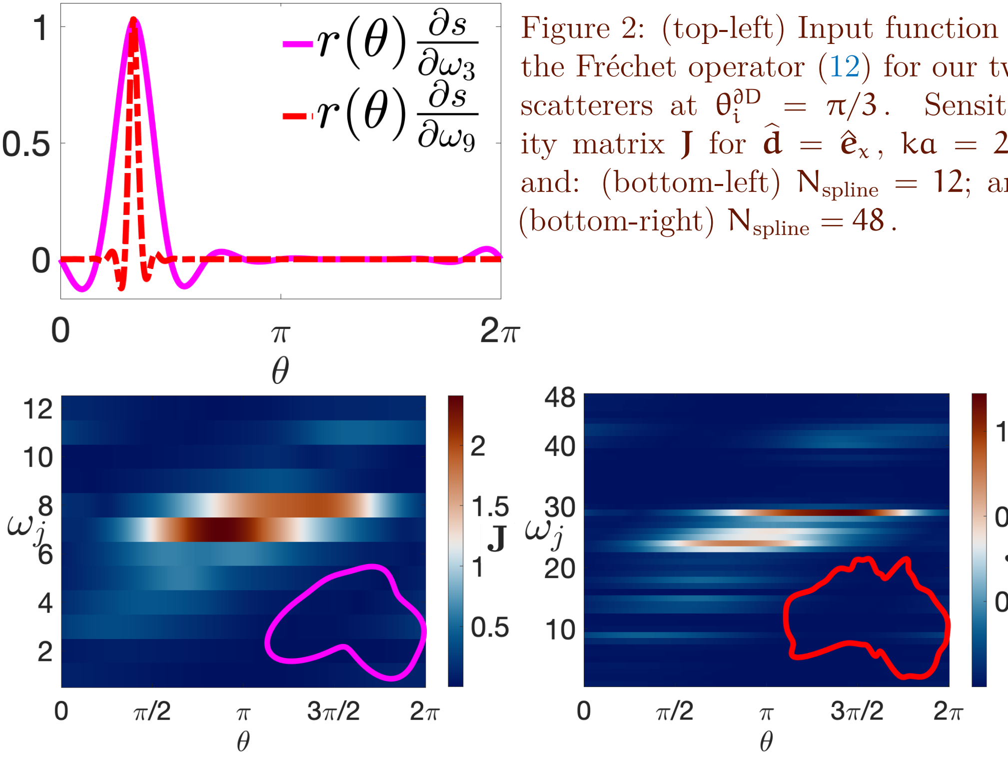

Figure 2: (top-left) Input function to the Fréchet operator (12) for our two scatterers at $\theta_i^{\partial D} = \pi/3$. Sensitivity matrix $\mathbf{J}$ for $\widehat{\mathbf{d}} = \hat{\mathbf{e}}_x$, $ka = 2\pi$, and: (bottom-left) $N_{\text{spline}} = 12$; and (bottom-right) $N_{\text{spline}} = 48$.

(bottom left and right) visualise the sensitivity matrix for a single incident wave with direction $\widehat{\mathbf{d}} = \hat{\mathbf{e}}_x$ and $ka = 2\pi$. Here we use $N_{\text{obs}} = 1000$ and Nyström parameter $m = 27$ and 240, for $N_{\text{spline}} = 12$ and 48, respectively, with the higher order quadrature required in the latter case to resolve the more complex geometry. These sensitivity plots contain key physical information, but the interplay between incident direction, observation angle, and geometric features makes interpretation challenging. We focus on these effects below, making use of (15).

Next we consider the case of four incident waves with $\widehat{\mathbf{d}} = \pm\hat{\mathbf{e}}_x, \pm\hat{\mathbf{e}}_y$. In Figures 3 and 4 we visualise the left (or shape) and right (or far-field) singular vectors for the largest three singular values for $ka = 2\pi, 4\pi, 6\pi$. We note that increasing ka dictates a slower rate of decay of the singular values. We visualise the shape singular vectors $|\mathbf{u}_i|$ using colour on the scatterer boundary. For the far-field singular vectors $|\mathbf{v}_i|$ visualisation, we plot the associated acoustic cross section $|\mathbf{v}_i|^2$ in polar coordinates. Since we have four incident waves, there are four associated cross sections, discriminated by color. The far-field singular vectors are normalised by σ_i so that the size of the perturbation in the far-field for a given shape perturbation can be quantified. For example, in the top-right plots of both figures the far-field is close to zero (the inner circle), indicating that the far-field is not very sensitive to the third shape singular vector.

These modes provide insight into which boundary features are most visible from far-field data across all incident waves. The most noticeable feature is that the support of the first shape singular vector is in all cases associated with the south-western tip of Western Australia. The corresponding far-field singular vectors show that this feature produces large perturbations in the far-field for those incident waves that illuminate it.

The shape singular vectors in Figure 3 show that most boundary regions contribute significantly to the far-field pattern, with the notable exception of the concave region in the southern tip corresponding to $\theta_{10}^{\partial D}$, where the sensitivity is markedly lower. This low sensitivity region represents a source of ill-posedness: two scatterers that differ only by small perturbations in ω_{10} may produce nearly indistinguishable far-field patterns, making accurate reconstruction of this geometric feature challenging. Figure 4 shows the same analysis as Figure 3 but for the finer discretization with $N_{\text{spline}} = 48$. In this case, the situation is significantly more complex, with many more identifiable regions with small sensitivity. This is nevertheless expected, since the finer geometric details introduced by the higher spline resolution are smaller than the wavelength scale at these ka values, placing them below the *diffraction limit* and therefore making them invisible in the far-field pattern.

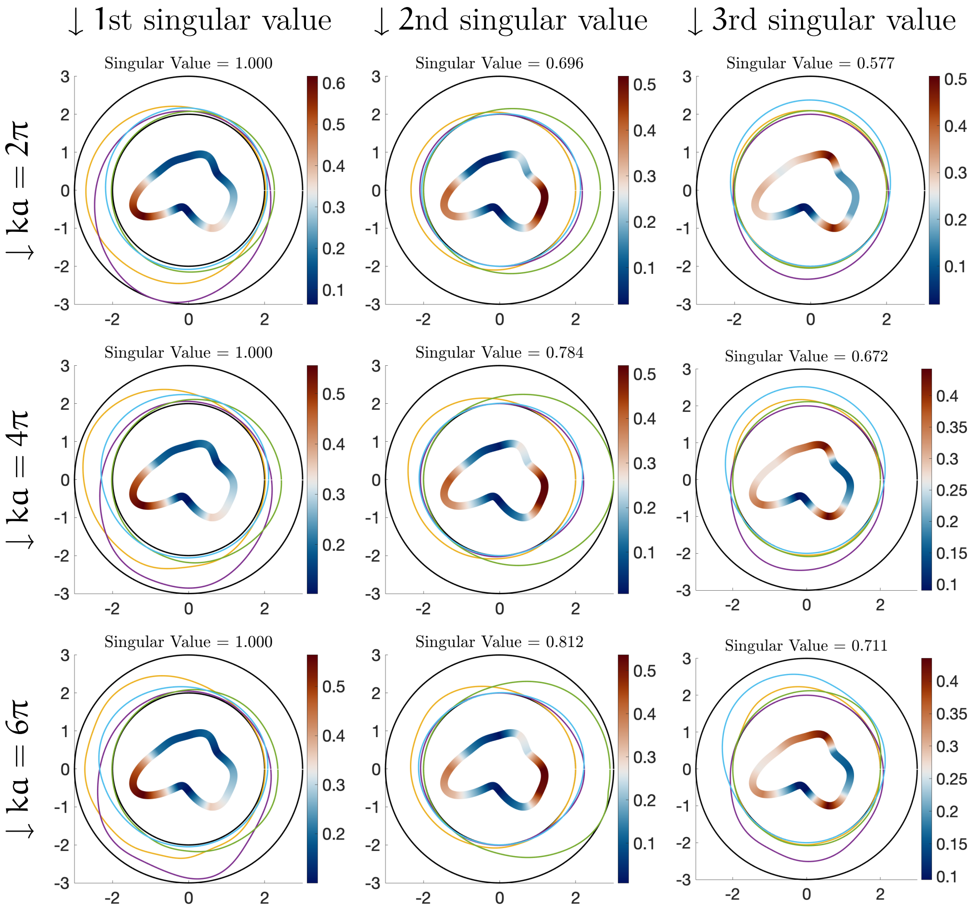

Figure 3: Visualisation of the first three singular values and associated left (shape) and right (far-field) singular vectors for $N_{\mathrm{spline}} = 12$ and J comprising of four incident waves with $\hat{\mathbf{d}} = \pm\hat{\mathbf{e}}_x, \pm\hat{\mathbf{e}}_y$.

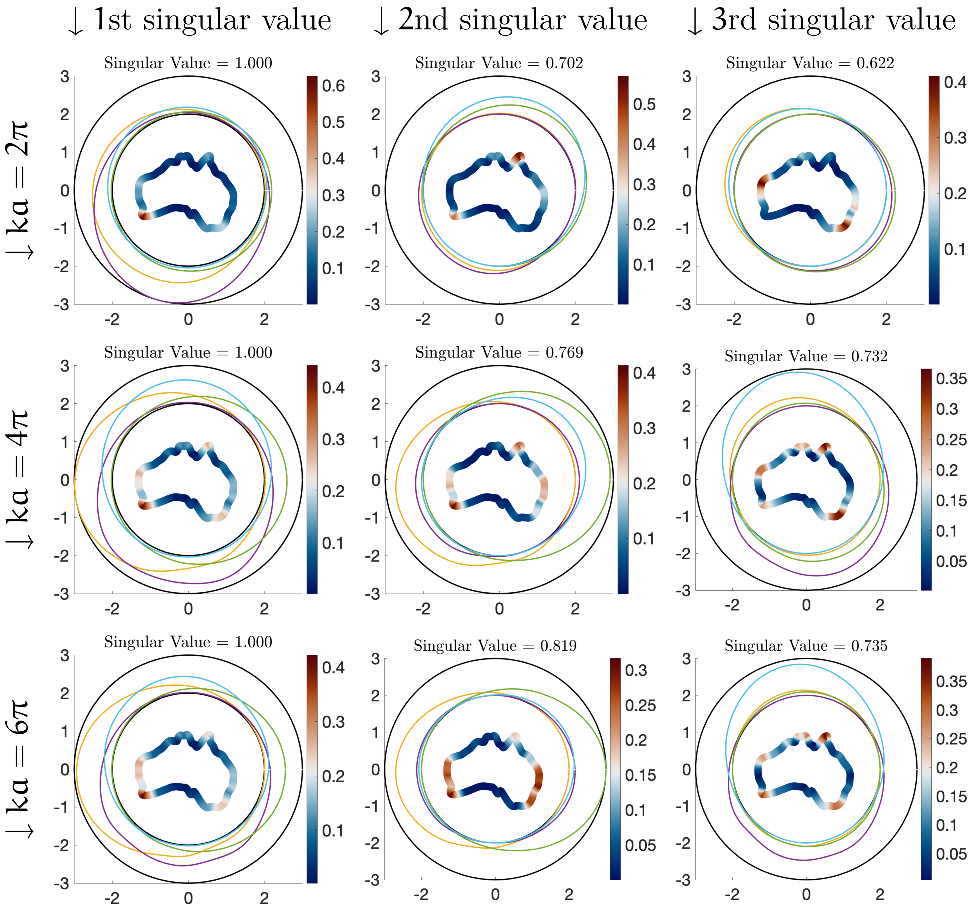

Figure 4: Visualisation of the first three singular values and associated left (shape) and right (far-field) singular vectors for $N_{\text{spline}} = 48$ and $\mathbf{J}$ comprising of four incident waves with $\widehat{\mathbf{d}} = \pm\hat{\mathbf{e}}_x, \pm\hat{\mathbf{e}}_y$.

5 Conclusions

We have provided an investigation of the effects of local perturbations to a given 2D scatterer's shape in corresponding far-field patterns. These effects can be written in terms of the Fréchet derivative $\mathrm{d}\mathcal{F}[\cdot]/\mathrm{d}r$ of the far-field operator with N_{spline} localised input functions following from a splines representation for the scatterer. The computation reduces to a coupled BIE which is accurately solved using the Nyström method. Upon choosing observation directions, all results can be represented through a sensitivity matrix $\mathbf{J}$ which we show can conveniently be studied using its SVD. This tool gives us useful information into the ill-posedness of the inverse problem such as which shape deformations can be reliably recovered from far-field data and which are effectively invisible to far-field measurements.

Acknowledgements The authors gratefully acknowledge M. Ganesh for discussions that substantially contributed to this work. They also acknowledge support from the Australian Research Council (ARC) through the Discovery Project Grant DP220102243.

References

[1] C. Borges and M. Rachh. "Multifrequency inverse obstacle scattering with unknown impedance boundary conditions using recursive linearization". In: *Adv. Comput. Math.* 48, 2 (2022). DOI: `10.1007/s10444-021-09915-1` (cit. on p. C117).

[2] M. Born and E. Wolf. *Principles of optics: Electromagnetic theory of propagation, interference and diffraction of light.* Elsevier, 2013. DOI: `10.1017/CBO9781139644181` (cit. on p. C117).

[3] D. Colton and R. Kress. *Inverse acoustic and electromagnetic scattering theory.* 4th ed. Springer, 2019. DOI: `10.1007/978-3-030-30351-8` (cit. on pp. C117, C118, C121, C122).

[4] M. Ganesh and S. C. Hawkins. “Algorithm 975: TMATROM—a T-matrix reduced order model software”. In: *ACM Trans. Math. Softw. (TOMS)* 44.1 (2017), pp. 1–18. DOI: `10.1145/3054945` (cit. on p. C122).

[5] M. Ganesh, S. C. Hawkins, N. Kordzakhia, and S. Unicomb. “An efficient Bayesian neural network surrogate algorithm for shape detection”. In: *Proceedings of the 19th Biennial Computational Techniques and Applications Conference, CTAC-2020.* Ed. by W. McLean, S. Macnamara, and J. Bunder. Vol. 62. ANZIAM J. 2022, pp. C112–C127. DOI: `10.21914/anziamj.v62.16110` (cit. on pp. C117, C118).

[6] F. Hettlich. “Fréchet derivatives in inverse obstacle scattering”. In: *Inv. Prob.* 11.2 (1995), p. 371. DOI: `10.1088/0266-5611/11/2/007` (cit. on p. C121).

[7] S. H. Schot. “Eighty years of Sommerfeld’s radiation condition”. In: *Hist. Math.* 19.4 (1992), pp. 385–401. DOI: `10.1016/0315-0860(92)90004-U` (cit. on p. C120).

[8] Z. Yang, X. Gui, J. Ming, and G. Hu. “Bayesian approach to inverse time-harmonic acoustic obstacle scattering with phaseless data generated by point source waves”. In: *Comput. Meth. Appl. Mech. Eng.* 386, 114073 (2021). DOI: `10.1016/j.cma.2021.114073` (cit. on pp. C117, C118).

Author addresses

1. **E. García Neefjes**, School of Mathematical and Physical Sciences, Macquarie University, Sydney NSW 2109, Australia.
`mailto:erik.garcia@mq.edu.au`

2. **S. C. Hawkins**, School of Mathematical and Physical Sciences, Macquarie University, Sydney NSW 2109, Australia.